Stationary Frame Current Control Evaluations for Three-Phase Grid-Connected Inverters with PVR-based Active Damped LCL Filters

Han, Yang; Shen, Pan; Guerrero, Josep M.

Published in:
Journal of Power Electronics

DOI (link to publication from Publisher):
10.6113/JPE.2016.16.1.297

Publication date:
2016

Document Version
Early version, also known as pre-print

JPE ??-?-?

http://dx.doi.org/10.6113/JPE.2014.14.1.???
ISSN(Print): 1598-2092 / ISSN(Online): 2093-4718

Stationary Frame Current Control Evaluations for Three-Phase Grid-Connected Inverters with PVR-based Active Damped LCL Filters

Yang Han †, Pan Shen*, and Josep M. Guerrero**

*†[1]Department of Power Electronics, School of Mechatronics Engineering, University of Electronic Science and Technology of China, No. 2006, Xiyuan Avenue, West High-Tech Zone, Chengdu 611731, China
[2]State Key Laboratory of Power Transmission Equipment & System Security and New Technology, Chongqing University, Chongqing 400044, China
[3]Artificial Intelligence Key Laboratory of Sichuan Province, Sichuan University of Science and Engineering, Zigong 643000, China
**Department of Energy Technology, Aalborg University, Aalborg 9220, Denmark

Abstract

Grid-connected inverters (GCIs) with LCL output filter have the ability of attenuating high-frequency (HF) switching ripples. However, by using only grid-current control, the system is prone to resonances if it is not properly damped, and the current distortion would be amplified significantly under highly distorted grid conditions. In this paper, a synchronous reference frame equivalent proportional-integral (SRF-EPI) controller in $\alpha\beta$ stationary frame using the parallel virtual resistance-based active damping (PVR -AD) strategy for grid-interfaced distributed generation (DG) systems to suppress the LCL resonance is proposed. Although both proportional-resonant (PR) controller in $\alpha\beta$ stationary frame and PI controller in dq synchronous frame achieve zero steady-state error, the amplitude- and phase-frequency characteristics differ greatly from each other except for the reference tracking at fundamental frequency. Therefore, an accurate SRF-EPI controller in $\alpha\beta$ stationary frame is established to achieve precise tracking accuracy. Moreover, the robustness, harmonic rejection capabilities, and influence of control delay are investigated by the Nyquist stability criterion when the PVR-based AD method is adopted. Furthermore, the grid voltage feed-forward and multiple PR controllers are integrated in the current loop to mitigate the current distortion introduced by the grid background distortion. Besides, the parameters design guidelines are presented to show the feasibility and effectiveness of the proposed strategy. Finally, simulation and experimental results are provided to validate the feasibility of the proposed control approach.

Key words: Synchronous frame equivalent PI, active damping, stability, LCL filter, PVR-AD scheme

I. INTRODUCTION

Recently, distributed generation (DG) systems based on renewable energy systems, such as photovoltaics and wind turbines, are attracting more and more attention. These renewable energy sources are usually installed in a distributed way and as an interface between DGs and the network, a grid-connected inverter (GCI) plays an important role in ensuring high-quality power to be injected to the grid [1-4].

In a GCI, an *L* filter or an *LCL* filter is usually used as an interface between the inverter and the grid. However, if only an inductor is used, high-frequency (HF) switching is needed to ensure that no excessive switching ripples are generated from the pulse-width modulation (PWM) process, which would be accompanied by undesirable problems of excessive switching losses and electromagnetic interference (EMI), especially in high-power applications [5]. Compared to the classical *L* filter, an *LCL* filter has better attenuation capacity of the switching harmonics and better dynamic characteristics,

Manuscript received April 29, 2015; accepted July 24, 2015
Recommended for publication by Associate Editor *****
†Corresponding Author: hanyang_facts@hotmail.com
Tel: +86-13730606846, Fax: +86-28-6183-0229, UESTC
*Dept. of Power Electronics, School of Mechatronics Eng., University of Electronic Science and Technology of China (UESTC), Chengdu, China

which usually yields to a lower volume and cost [6]. However, the *LCL* filter is a three-order system and instability problems may occur at the resonant frequency, thus proper damping solutions are mandatory to stabilize the whole system [7].

The ways to damp the resonance problems can be classified into passive damping (PD) and active damping (AD) methods. PD is achieved by inserting an additional resistor in series or parallel with the filter inductor or filter capacitor [8]. The PD scheme by adding a resistor in series with the filter capacitor has been widely adopted for its simplicity and highly reliability. However, the additional resistor will result in power loss and decrease the attenuation of the LCL filter [9]. In order to overcome these drawbacks, the concept of virtual resistor was proposed, which is called AD method [10], [11]. And an interesting control strategy based on the feedback of the splitting capacitor current was proposed in [12]. With this method, the injected current is not controlled directly and the damping capability relies on the LCL parameters. Therefore, among the AD methods, the method involving feedback of the capacitor current has attracted considerable attention due to its simple implementation and wide application [2], [13-17].

Another interesting approach, which is the main focus of this work, is to consider the current controller implementation so that a better performance is ensured. It is well-known that the proportional integral (PI) controller has an infinite gain for dc component, thus guarantees a precise tracking for dc references without steady-state error. However, for ac references, the PI controller would lead to steady-state error due to the finite gain at the selected frequency [18], [19]. The proportional resonant (PR) controller can provide infinite gain at the selected resonant frequency to suppress the effect of the unwanted harmonics, thus ensuring zero steady-state error when tracking an ac reference at the selected frequency [20-22]. On the other hand, by applying PI controller in *dq* synchronous frame can ensure zero steady-state error, since the ac signal is transformed into dc signal, thus infinite gain is achieved by the PI controller at the dc component [23], [24]. However, the synchronous frame PI control scheme requires accurate phase synchronization of the grid voltage by using a phase-locked-loop (PLL), which may deteriorate the tracking performance under grid disturbances [24]. Moreover, the straightforward analysis method which is named PI model, i.e., to replace the PI controller in *dq* synchronous frame with PI plus resonant controller in *αβ* stationary frame. However, the approximation is not accurate and the coupling terms are ignored, either [25]. In [26], an accurate synchronous frame equivalent PI (SRF-EPI) in stationary frame with *L* filter was presented, which shows robust performance under a wide frequency range. However, the system with the *LCL* resonance is not considered and the effects of the power-stage parameter deviations and the grid background distortion were not taken into account, and the discrete model and the control delay effect were also neglected.

This paper proposes a novel parallel virtual resistance (PVR)-based AD method integrated with the SRF-EPI control strategy in *αβ* stationary frame for three-phase grid-connected inverter with an LCL filter. The multiple PR controllers and the grid voltage feed-forward loop for improving tracking precision under background grid distortion conditions are investigated when the proposed strategy is used. Moreover, the SRF-EPI, PI and PR controllers are analyzed, designed and compared, which show the feasibility and effectiveness of the proposed strategy.

This paper is organized as follows. In Section II, the system description and the proposed control scheme are presented. The damping characteristics of the various PD schemes, the series virtual resistance (SVR)- and PVR-based AD strategies are analyzed, and the use of the SRF-EPI, PI and PR controllers are compared in the stationary frame. Section III presents the parameters design guidelines. The impact of LCL-parameter variations based on the SRF-EPI controller in the stationary frame is studied as well. Section IV presents the simulation and experimental results of a 2.2 kVA three-phase DG system. Finally, Section V concludes this paper.

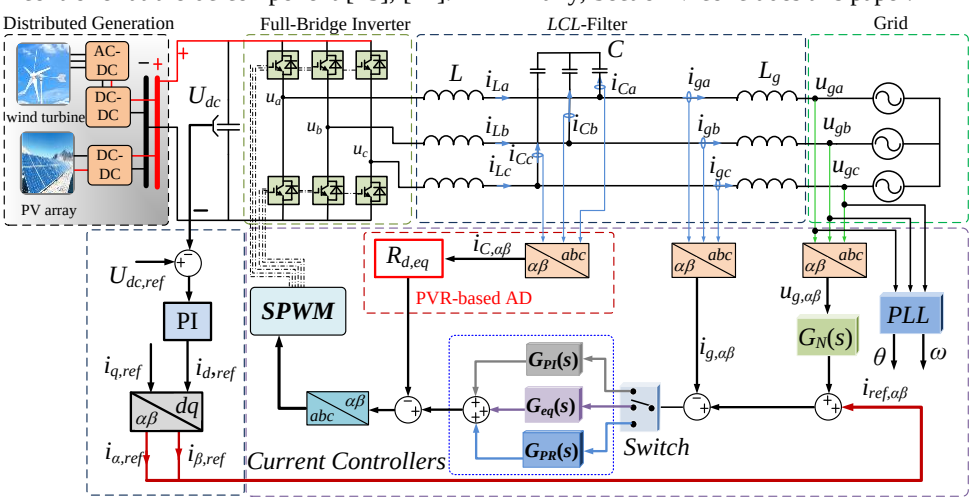

Fig. 1. System topology and control strategy of the three phase grid-connected inverters with *LCL* filter.

II. System Description and Control Scheme

Fig. 1 shows the topology of three-phase grid-connected voltage source inverter (VSI) based on the LCL filter, where the inductor parasitic resistances are neglected. In addition, the switch is used to choose the current controllers and $G_{PI}(s)$, $G_{eq}(s)$, and $G_{PR}(s)$ correspond to the PI controller, the SRF-EPI controller, and the PR controller, respectively. To achieve a good filtering performance, the resonance frequency of LCL filter should be in the range of $10f_0<f_{res}<(f_s/2)$, where f_0 denotes the fundamental frequency, f_{res} represents the resonance frequency, and f_s is the switching frequency [7], [18], [27]. Based on these guidelines, the parameters of the power-stage are given in Table I.

TABLE I
System Parameters of the LCL Grid-Tied Inverter

Symbol	Quantity	Value
U_{dc}	Input voltage amplitude	650 V
u_g	Grid voltage	311 V
T_s	Sampling and switching period	100 μs
ω_0	Fundamental angular frequency	100π *rad/s*
C	Capacitor	10 μF
L	Converter-side inductor	1.8 *m*H
L_g	Grid-side inductor	1.8 *m*H

A. Stationary Frame SRF-EPI, PI and PR Controllers

A major objective for ac current regulators is to achieve zero phase and magnitude errors. Here, the synchronous reference frame equivalent PI (SRF-EPI) controller in the stationary frame was presented as an alternative solution for fundamental frequency reference signal tracking purposes [26], [28].

The synchronous reference frame equivalent integral controller is $F\angle\theta$, and $n<0$ means the signal is in negative sequence.

$$F=\begin{cases}\infty & n=1\\ \dfrac{2k_i}{\omega_0|n-1|} & n\neq 1\end{cases},\quad \theta=\begin{cases}0^\circ & n=1\\ -90^\circ & (n>1)\bigcup(n<0)\\ 90^\circ & 0<n<1\end{cases} \tag{1}$$

The proportional (P) controller in dq synchronous frame is the same as the P controller in the $\alpha\beta$ frame. Then, the SRF-EPI controller transfer function is

$$G_{eq}(s)=k_P+F\angle\theta=k_P+F\cos\theta+jF\sin\theta \tag{2}$$

Compared with the SRF-EPI controller, the integral and resonant models of PI and PR models are given by

$$F_I=\begin{cases}\infty & n=0\\ \dfrac{k_i}{\omega_0 n} & n\neq 0\end{cases},\quad \theta_I=-90^\circ \tag{3}$$

$$F_R=\begin{cases}\infty & n=1\\ \dfrac{2k_i}{\omega_0^2(n^2+1)} & n\neq 1\end{cases},\quad \theta_R=\begin{cases}0^\circ & n=1\\ -90^\circ & n>1\\ 90^\circ & n<1\end{cases} \tag{4}$$

The PI and PR current controller are obtained by substituting (3) and (4) into (2), respectively.

Fig. 2 shows the bode plots of the equivalent model G_{eqI}, the resonant and integral controllers for the fundamental frequency signal tracking. It can be seen that the models show remarkable differences from each other in the low frequency range, thus the direct implementation of the PR or PI model to predict system performance would lead to inaccurate result. As for the phase characteristic, equivalent PI controller G_{eqI} in positive sequence shows the same phase characteristic with resonant model, while G_{eqI} in the negative sequence shows the same phase-frequency characteristic with integral model.

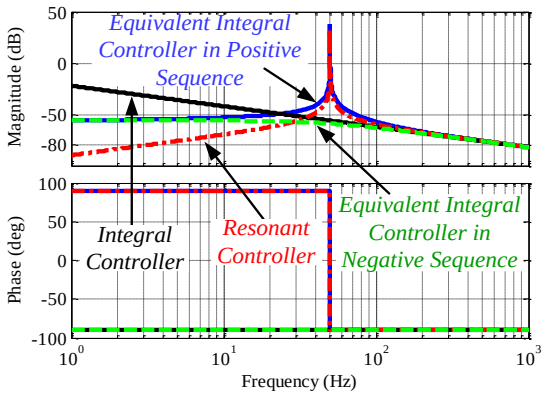

Fig. 2. Bode plots of the integral controller, resonant controller, and equivalent integrator controller in positive and negative sequences.

B. Passive Damping under Grid Current Feedback

As shown in Fig. 3, the grid current is conventionally used as a feedback variable of the current controller to regulate the current injected into the grid. An amplitude peak exists at the resonant frequency of the LCL filter, which would limit the design procedure of the current control-loop [6], [29].

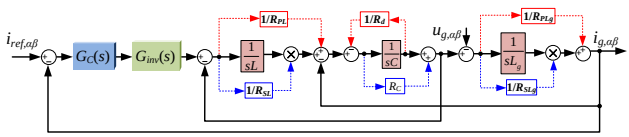

Fig. 3. Block diagram of various PD methods under grid current control for the three-phase inverter with *LCL* output filter.

The direct way to damp the LCL filter resonance is to insert a passive resistor in the inductor or capacitor of the *LCL* filter. In this case, the open-loop transfer functions of the grid current feedback control algorithm with various passive damping (PD) methods can be obtained as

$$\begin{cases}G_{Series-L}(s)=\dfrac{G_C(s)G_{inv}(s)}{s^3LL_gC+s^2CL_gR_{SL}+s(L+L_g)+R_{SL}}\\ G_{Series-L_g}(s)=\dfrac{G_C(s)G_{inv}(s)}{s^3LL_gC+s^2CLR_{SL_g}+s(L+L_g)+R_{SL_g}}\end{cases} \tag{5}$$

$$\begin{cases}G_{Parallel-L}(s)=\dfrac{G_C(s)G_{inv}(s)(sL+R_{PL})}{s^3LL_gCR_{PL}+s^2LL_g+sR_{PL}(L+L_g)}\\ G_{Parallel-L_g}(s)=\dfrac{G_C(s)G_{inv}(s)(sL_g+R_{PL_g})}{s^3LL_gCR_{PL_g}+s^2LL_g+sR_{PL_g}(L+L_g)}\end{cases} \tag{6}$$

$$G_{Series-C}(s)=\frac{G_C(s)G_{inv}(s)(sCR_C+1)}{s^3LL_gC+s^2CR_C(L+L_g)+s(L+L_g)} \quad (7)$$

$$G_{Parallel-C}(s)=\frac{G_C(s)G_{inv}(s)R_d}{s^3LL_gCR_d+s^2LL_g+sR_d(L+L_g)} \quad (8)$$

where $G_{inv}(s)=U_{dc}/U_{tri}$ is the gain of the PWM inverter, U_{dc} is the inverter dc voltage, and $U_{tri}=1$ is the carrier amplitude. $G_{Series\text{-}L}$ and $G_{Series\text{-}Lg}$ represent the open-loop transfer functions from $i_{ref,\alpha\beta}$ to $i_{g,\alpha\beta}$ when damping resistor is connected in series with L and L_g, respectively. $G_{Parallel\text{-}L}$ and $G_{Parallel\text{-}Lg}$ represent the open-loop transfer functions when the damping resistor is connected in parallel with L and L_g, respectively. $G_{Series\text{-}C}$ and $G_{Parallel\text{-}C}$ are the open-loop transfer functions when damping resistor is connected in series and parallel with C, respectively.

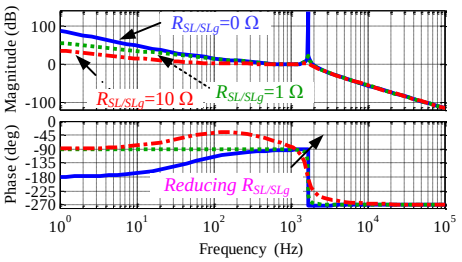

(a)

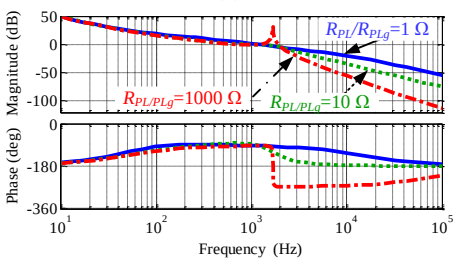

(b)

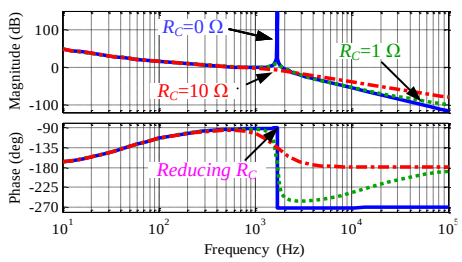

(c)

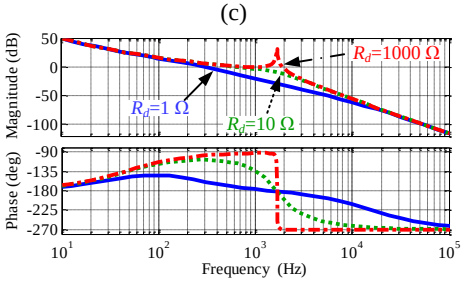

(d)

Fig. 4. Bode plots of the open-loop transfer function under grid current feedback control with various PD methods (Magnitude, phase are abbreviated as *Mag*, *Ph*). (a) The resistor in series with L or L_g. (b) The resistor in parallel with L or L_g. (c) The resistor in series with C. (d) The resistor in parallel with C.

Fig. 4 shows the bode plots of the open-loop transfer functions with various PD schemes using the parameters in Table I when a PI current regulator is used. As shown in Fig. 4(a), the LCL filter with PD methods has less attenuation in the low frequency (LF) region when a series resistor is connected with L or L_g. The less attenuation is caused in the HF region when a parallel resistor is connected with L or L_g which is shown in Fig. 4(b). As shown in Fig. 4(c), it can be seen that the less attenuation is also caused when a series resistor is connected with C. As shown in Fig. 4(d), there is no impact on the LF and HF regions when a parallel resistor is connected with C. However, an excessive power loss is always existing among the various PD schemes.

C. Virtual Resistance based Active Damping (AD) Strategy

Compared with PD method, active damping (AD) strategy is more flexible and more efficient, which adopts virtual resistor to eliminate power loss and can be easily incorporated to the existing control algorithm. The block diagram transformation of traditional virtual resistor in series with capacitor is derived in Fig. 5. It is reported that, the series virtual resistance based AD (SVR-based AD) needs to introduce differential element and it will cause noise amplification problems and the system can be unstable due to HF interference [17].

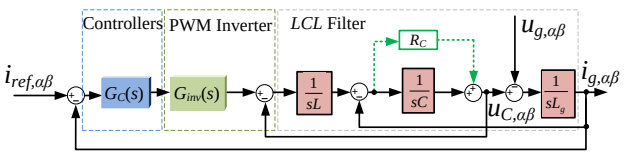

(a)

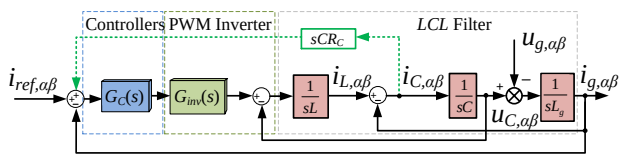

(b)

Fig. 5. Block diagram transformation of virtual resistor in series with capacitor. (a) Passive damping of capacitor series with resistor. (b) Equivalent SVR-based AD.

Therefore, an effective parallel virtual resistance based active damping (PVR-based AD) method in parallel with capacitor for LCL filter is proposed in this paper, which avoids the LCL resonance problems, and the satisfactory stability and robustness can be achieved. The principle diagram and its block diagram transformations of PVR-based AD are shown in Fig. 6.

The transfer function of the PVR-based AD describing the grid current $i_{g,\alpha\beta}$ as a function of voltage $u_{s,\alpha\beta}$ is given by

$$G_{active-i_g u_s}(s)=\frac{i_{g,\alpha\beta}(s)}{u_{s,\alpha\beta}(s)}=\frac{1}{s(LL_gCs^2+R_{d,eq}L_gCs+(L+L_g))} \quad (9)$$

where $R_{d,eq}$ is an equivalent proportional term, $R_{d,eq}=L/(CR_d)$.

According to Fig. 6(b), the open-loop transfer function of the PVR-based AD is given by

$$G_{open}(s)=\frac{G_C(s)G_{inv}(s)}{LL_gCs^3+R_{d,eq}L_gCs^2+(L+L_g)s} \quad (10)$$

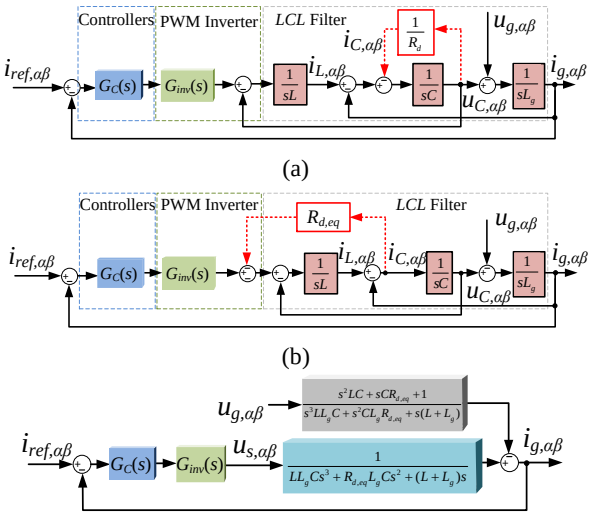

Fig. 6. Block diagram transformations of the PVR-based AD method. (a) PD scheme using parallel-connected resistor across capacitor. (b) Block transformation of PD control strategy in (a). (c) The block diagram of parallel virtual resistance active damping.

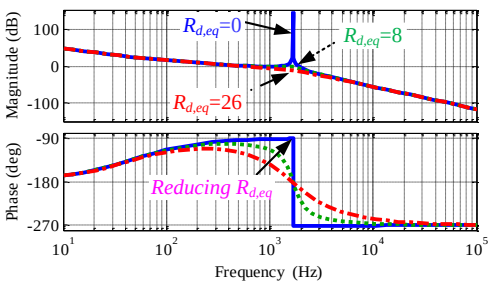

Fig. 7. Bode plots of the open-loop transfer function with PVR-based AD strategy.

From (10), it shows that there is no unstable open-loop poles, i.e., P=0. If the PI current controller is used, by using the parameters in Table I, the bode plots of the open-loop transfer function $G_{open}(s)$ with AD method when $R_{d,eq}$ is 0, 8 and 26 is illustrated in Fig. 7, respectively. The corresponding parallel virtual resistor R_d is ∞, 22.5 Ω and 6.9 Ω, respectively. According to Nyquist stability criterion [7], the system is stable if Q=0

$$Q=P+N_+-N_- \quad (11)$$

where P is the number of unstable open-loop poles, N_+ and N_- are the number of times that the path crosses the line in the clockwise and counter-clockwise directions. Hence, there is a one-to-one correspondence between positive half of Nyquist plot and the open-loop bode plot, and the N_+ and N_- are two times the numbers of positive (from lower to upper) and negative (from upper to lower) crossings of $(2k+1)\pi$ (k is an integer) in the open-loop bode plot in the frequency range with gains above 0 dB. For minimum phase system, i.e., P=0, the system is stable if N_+=N_- [29], [30].

1) When $R_{d,eq}$ =0, the *PH-F* contour cross -180 ° from upper to lower at f_{res} (in *Mag*>0 dB region). Thus, when P=0, N_-=0, N_+=2, and Q=2, the system is unstable.
2) When the feedback gain $R_{d,eq}$ increases, the *PH-F* contour cross -180 °outside the *Mag*>0 dB region if the value of $R_{d,eq}$ is appropriate. Thus, when P=0, N_-=0, N_+=0, and Q=0, the system is stable. The case for $R_{d,eq}$ =0, 8, 26 is shown in Fig. 8, respectively.

In order to intuitively show variation tendency of system stability when $R_{d,eq}$ varies, the discrete pole-zero map for feedback gains $R_{d,eq}$ increases from 0 to 36 is illustrated in Fig. 8 by using the ZOH method. It can be seen that the system stability changes along with delay time. The discrete open-loop transfer function of current controller using PVR-based AD scheme is

$$G_{open}(z)=G_C(z)\times Z\left[G_d(s)G_{inv}(s)\frac{1-e^{-sT_s}}{s}\times\frac{1}{LL_gCs^3+R_{d,eq}L_gCs^2+(L+L_g)s}\right] \quad (12)$$

$$G_d(s)=e^{-sT_d} \quad (13)$$

where $G_d(s)$ represents the delay in digital control, T_d is delay time and it is related with analog-digital sampling process, PWM generation process, and hardware filtering [6], [26], [30]. The PWM switching frequency and the sampling frequency of the digital current controller are both selected to be 10 kHz.

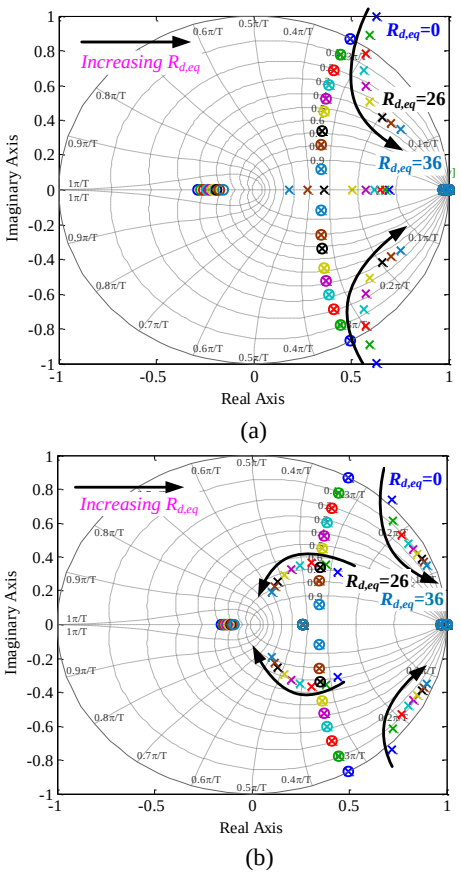

Fig. 8. Pole-zero map for close-loop transfer function with PVR-based AD strategy. (a) No delay. (b) $3/2T_s$ delay

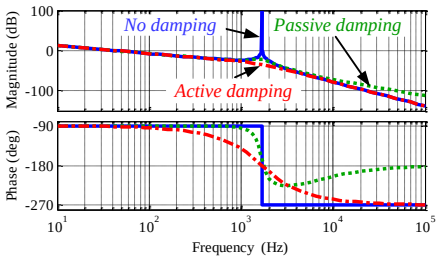

Fig. 9. Bode plots of PVR-based AD scheme compared with PD and no damping strategies.

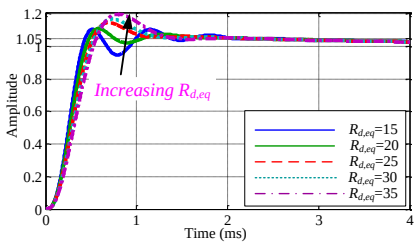

Fig. 10. Step response of the PVR-based AD scheme with different $R_{d,eq}$.

Fig. 9 shows the frequency domain comparison among the PVR-based AD strategy, PD method and no damping scenario. It can be observed from Fig. 7 and Fig. 9 that the PVR-based AD method ensures effective damping characteristics and the attenuations in LF and HF regions are not affected, which is an advantage over the various PD methods.

Once again referring to Fig. 8, it can be seen that either too small or too large $R_{d,eq}$ values will affect the stability of the system. By gradually increasing $R_{d,eq}$, the poles can be moved close to the center of the unit circle. However, the poles will be moved away from the circle when $R_{d,eq}$ continues increasing, reducing the stability margin and leading to instabilities. Hence, it is necessary to optimize the damping coefficient $R_{d,eq}$, thus ensuring that system has sufficient stability margin and good dynamic performance.

Equation (9) is equivalent to a first order model combined with a second order plant model, and the resonance is caused by the second order system. Notably, the resonance of the second- order system is determined by the damping ratio ξ. The damping ratio ξ in (9) is shown in (14). To eliminate the resonance, let ξ=0.707, thus the feedback gain is calculated as $R_{d,eq}$=26.8, i.e., the parallel virtual resistor R_d is 6.7 Ω.

$$\xi = \frac{R_{d,eq}}{2L\omega_{res}} = \frac{R_{d,eq}}{2}\sqrt{\frac{L_g C}{(L+L_g)L}} \tag{14}$$

Fig. 10 shows the step responses of PVR-based AD method with different $R_{d,eq}$ scenarios. It can be seen that the dynamic response is influenced by the value of $R_{d,eq}$. The overshoots as well as the oscillations are largely reduced with increasing $R_{d,eq}$ and the settling time is the shortest while $R_{d,eq}$=26.8. In summary, the optimal performance is achieved when $R_{d,eq}$ equals 26.8, and changes along with the delay time.

D. Grid Voltage Disturbance Rejection

To mitigate the effect of the grid voltage distortion on the quality of output currents of the LCL-filter, the proportional-resonant (PR) was introduced to provide infinite gain at the selected harmonic frequencies to guarantee the sinusoidal grid currents [22], [31]. The method based on the concept of harmonic impedance, which is to incorporate the grid voltage harmonics in the control loop through an additional feed-forward path could also suppress the effects of the unwanted harmonics, would not affect the phase margin. However, the compensation accuracy of this approach is not satisfactory [32].

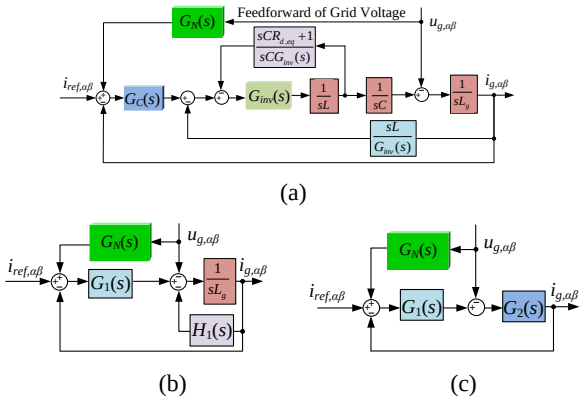

Fig. 11. Block diagram transformation of the PVR-based AD control algorithm with the grid voltage feed-forward loop.

The block diagram transformation of the PVR-based AD algorithm with the grid voltage feed-forward loop is shown in Fig. 11, and the current injected into the grid can be derived as

$$\begin{aligned} i_{g,\alpha\beta}(s) &= \frac{W(s)}{1+W(s)} i_{ref,\alpha\beta}(s) - \frac{1-G_N(s)G_1(s)}{1+W(s)} G_2(s) u_{g,\alpha\beta}(s) \\ &= i_{g1}(s) + i_{g2}(s) \end{aligned} \tag{15}$$

where

$$G_1(s) = \frac{G_C(s)G_{inv}(s)}{s^2LC + sCR_{d,eq} + 1} \tag{16}$$

$$G_2(s) = \frac{s^2LC + sCR_{d,eq} + 1}{s^3LL_gC + s^2CL_gR_{d,eq} + s(L+L_g)} \tag{17}$$

and $W(s)=G_1(s)G_2(s)$.

The transfer function from the grid voltage to the grid side current with PVR-based AD is derived as

$$\frac{i_{g,\alpha\beta}(s)}{u_{g,\alpha\beta}(s)} = \frac{s^2LC + sCR_{d,eq} + 1}{G_C(s)G_{inv}(s) + s^3LL_gC + s^2CL_gR_{d,eq} + s(L+L_g)} \tag{18}$$

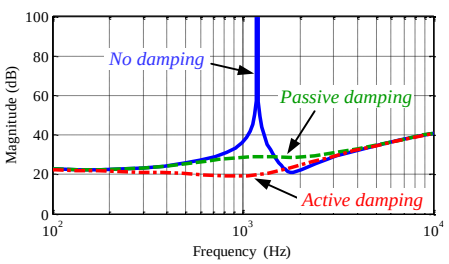

Fig. 12. Bode plots comparison of disturbance voltage to grid current of the harmonic admittance without the feed-forward of grid voltage.

Fig. 12 shows the bode plots of (18) under no damping, PD

and PVR-based AD cases without feed-forward of grid voltage. It can be observed that a voltage disturbance near the resonance frequency results in large input currents under no damping case. However, the PD and PVR-based AD schemes provide efficient resonance damping characteristics, and the PVR-based active damping scheme shows additional damping performance without causing additional power losses.

In order to mitigate the effect of the grid voltage on the quality of LCL-filter currents, a feed-forward loop of the grid voltage and the multiple resonant regulators at the harmonic frequencies of grid voltages are applied in the current loop. According to (15), setting 1-$G_N(s)G_1(s)$ to zero and adopting approximate full compensation approach, the feed-forward function is derived as

$$G_N(s)=\frac{1}{G_1(s)}=\frac{s^2LC+sCR_{d,eq}+1}{G_C(s)G_{inv}(s)} \tag{19}$$

Considering that derivative functions are difficult to be implemented and mainly for middle- and higher-frequency harmonics, and the noise amplification problems would reduce the stability margin, hence (19) is approximated by a first order low pass filter, and the higher order differential terms are neglected to avoid high frequency instabilities [29], [33]. As shown in Fig. 11(a), if the feed-forward control lies behind the current controller, the feed-forward factor has a very simple form and the proportional feed-forward is adopted, and $G_N(s)=1/G_{inv}(s)$. Moreover, the multiple resonant controllers are achieved by paralleling several resonant blocks tuned to the desired harmonic frequencies to be compensated, which is expressed as

$$G_h(s)=\sum_{h=5,7,11...}\frac{2K_{ih}s}{s^2+(h\omega_0)^2} \tag{20}$$

where h is the harmonic order to be compensated, ω_0 represents the fundamental frequency, and K_{ih} represents the respective resonant gain, which should be tuned relatively high, but within the stability limits, for minimizing the steady-state error. The dynamics of the fundamental PI, PR and SRF-EPI controllers in the stationary frame is unaffected when the multiple resonant controllers are added, since the resonant controllers compensate only for frequencies that are very close to the selected resonant frequencies.

III. Design Guidelines

A. Stability of the SRF-EPI, PI and PR Controllers

The resonance damping and dynamic response have been taken into consideration for the aforementioned active damping design procedure. Thus, the current regulator $G_C(s)$ is designed to maintain suitable PM, GM and cutoff frequency f_c. Generally, PM in the range of 30°~60° and GM≥3~6 dB are adopted for a compromise among the stability, dynamic response and robustness [10], [14].

The cutoff frequency f_c is typically restricted lower than f_s, considering the effect of attenuating HF noise and f_c generally can be chosen lower than 1/10 of f_s. Therefore, considering the frequency response of the system below the cutoff frequency, the influence of the capacitor of LCL filter can be ignored and $G_{open}(s)$ can be approximated as

$$G_{open}(s)\approx\frac{G_C(s)G_{inv}(s)}{(L+L_g)s} \tag{21}$$

Here, PI controller is adopted to design the parameters for the PR controller and SRF-EPI controller for comparison. At the cutoff frequency, the magnitude-frequency characteristic of the open-loop system is zero, hence

$$20\lg\left|G(j2\pi f_c)\right|\approx 20\lg\left|\frac{k_pG_{inv}(s)}{(L+L_g)*j2\pi f_c}\right|=0 \tag{22}$$

Thus, the controller gain k_p is approximately represented as

$$k_p\approx\frac{2\pi f_c(L+L_g)}{G_{inv}(s)} \tag{23}$$

showing that f_c is approximately proportional to k_p. Therefore, a larger k_p means a faster dynamic response and a larger loop gain at low frequencies.

The steady-state error of $i_{g,\alpha\beta}$ at fundamental frequency $\omega_0=2\pi f_0$ is an important index of the controller parameters design. As given by (15), assuming adoption of grid feed-forward control, the steady-state tracking error of grid current $i_{g,\alpha\beta}$ can be calculated as

$$E_g(s)=\frac{i_{g1}(s)-i_{ref}(s)}{i_{ref}(s)}=\frac{W(s)}{1+W(s)}-1 \tag{24}$$

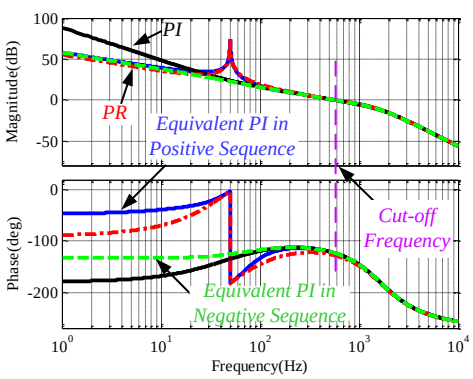

Fig. 13. Bode plots of the open-loop transfer function with PVR-based AD strategy.

The fundamental components of i_{g2} and $u_{g,\alpha\beta}$ are denoted by i_{g2}^* and u_g^*, respectively. As the influence of the filter capacitor is negligible at fundamental frequency f_0, considering (18), i_{g2}^* can be approximated as

$$i_{g2}^*\approx-\frac{u_g^*}{G_{inv}G_C(j2\pi f_0)} \tag{25}$$

Considering equation (21) and (25), I_{g2} can be derived as

$$I_{g2}\approx\frac{U_g}{G_{inv}\left|G_C(j2\pi f_0)\right|}\approx\frac{U_g}{2\pi f_0\left|G_{open2}(j2\pi f_0)\right|} \tag{26}$$

where I_{g2} and U_g are the root mean square (RMS) values of i_{g2}^* and u_g^*, respectively.

According to (21) and the transfer function of PI controller, (26) can be rewritten as

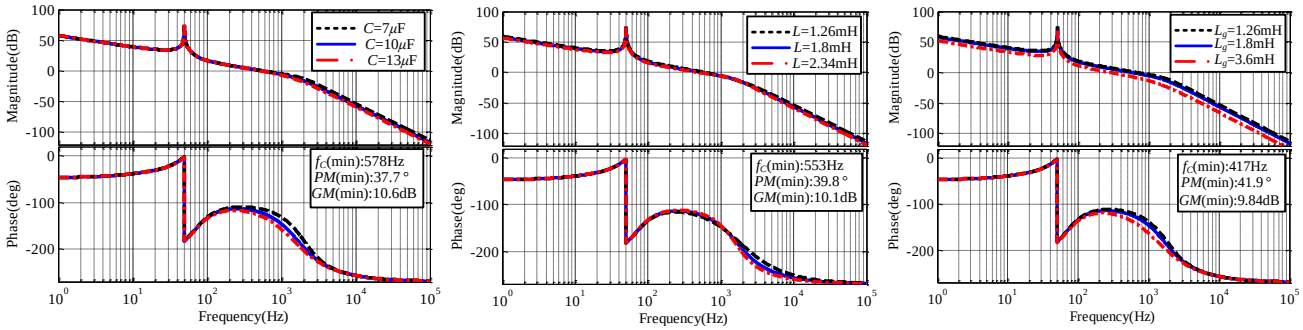

(a) (b) (c)

Fig. 14. Bode plots of the system considering the variations of the *LCL* filter parameters with PVR-based AD strategy. (a) *C*: 10 μF ±30%. (b) *L*: 1.8 mH ±30%. (c) L_g: 1.8 mH -30% ~ +100%.

$$G_{open2}(f_0)=20\lg\left|G_{open2}(j2\pi f_0)\right|=20\lg\left|\frac{G_{inv}(k_p+\frac{k_i}{j2\pi f})}{j2\pi f_0(L+L_g)}\right| \quad (27)$$

Substituting (23) into (27), the integration gain is derived as

$$k_i=\frac{4\pi^2 f_0(L+L_g)}{G_{inv}}\sqrt{(10^{\frac{G_{open2}(f_0)}{20}}f_0)^2-f_c^2} \quad (28)$$

According to (17) and (18), the PM of the system can be expressed as

$$PM=180^0+\angle\frac{G_C(s)G_{inv}(s)}{LL_gCs^3+R_{d,eq}L_gCs^2+(L+L_g)s}\bigg|_{s=j2\pi f_C} \quad (29)$$

Substituting the transfer function of PI into (29), and

$$PM=\arctan\frac{2\pi L(f_{res}^2-f_c^2)}{G_{inv}f_c}-\arctan\frac{k_i}{2\pi f_c k_p} \quad (30)$$

Then, (30) can be rewritten as

$$k_i=2\pi f_C k_p\frac{2\pi L(f_{res}^2-f_C^2)-G_{inv}f_C R_{d,eq}\tan PM}{2\pi L(f_{res}^2-f_C^2)\tan PM+G_{inv}f_C R_{d,eq}} \quad (31)$$

Using parameters of Table I, the resonance frequency f_{res} of *LCL* filter is equal to 1.68 kHz, and the value of the cutoff frequency f_C is selected as 600Hz. In addition, the PM is selected as 50 degrees. With the system parameters given in Table I, the SRF-EPI, PI and PR controller parameters are selected as k_p=0.02, k_i=5.77. The bode plots of the open-loop transfer function with PVR-based AD when $R_{d,eq}$ =26.8 is shown in Fig. 13. When PI compensator is adopted, the GM and PM are 11.1 dB and 52.2 degrees, respectively. When the equivalent model of synchronous-frame PI compensator in the stationary frame is adopted, the GM and PM are 11 dB and 44.9 degrees, respectively. When PR compensator is adopted, the GM and PM are 9.56 dB and 31.5 degrees, respectively.

As shown in Fig. 13, except for LF range, the open-loop bode plots of the stationary frame equivalent model of PI controller in positive sequence and PR model are the same at fundamental frequency, and similar in the HF range. Hence, indicating that the SRF-EPI controller in stationary frame has similar performance with PR controller in the stationary frame when tracking the fundamental frequency reference. Thus, the SRF-EPI controller has a better performance than the PI and PR controllers in all frequencies when they are used in stationary frame. Except for reference tracking at the fundamental frequency, the SRF-EPI controller in stationary frame is not equivalent to PI or PR controller in the $\alpha\beta$ fram

B. *Impacts of LCL-Parameter Variations*

In fact, filter parameters drift away from the rated values due to the parasitic parameters variations, the operating conditions, temperature and grid impedance impact [10], [34]. To examine the robustness of the system with PVR-based AD scheme of the SRF-EPI controller in the $\alpha\beta$ frame, the bode plots of the compensated loop gain considering the variations of the *LCL* filter parameters are given in Fig. 14. The grid impedance is considered as a part of L_g. It is found that, although *C* varies from 7 to 13 μF (10 μF ±30%), *L* varies from 1.26 to 2.34 mH (1.8 mH ±30%), or L_g varies from 1.26 to 3.6 mH (1.8 mH -30% ~ +100%), the lowest cutoff frequency is still higher than 417 Hz, the PM is larger than 37.7 degrees, the GM is larger than 9.84 dB. The frequency response characteristics in Fig.14 verify that the designed system has a strong robustness.

IV. Simulation and Experimental Results

In order to verify the effectiveness of the proposed control strategies, the simulation and experimental results of the proposed control strategy are presented and compared. The simulation studies were implemented using Matlab/Simulink. As shown in Fig. 15, the experimental setup was built and test, which consists of two 2.2 kW Danfoss inverters, one working as grid-connected inverter and the other controlled in voltage control mode to emulate the grid with distortion. The dSPACE1006 platform was used to implement the control algorithms. In order to provide effective comparison, all the control parameters are the same for the simulation and experiments. The system parameters are given in Table I and the SRF-EPI, PI and PR controllers parameters are selected as k_p=0.02, k_i=5.77.

Fig. 15 Experimental setup.

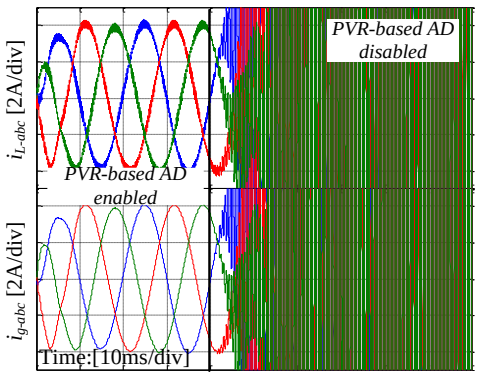

Fig. 16. Simulation result of the SRF-EPI control strategy when PVR-based AD strategy is disabled at 40ms.

Fig. 16 demonstrates the performance of the PVR-based AD strategy when the SRF-EPI controller is adopted. When PVR-based AD strategy is enabled, the system is stable without resonance. However, when active damping is disabled, resonance appears and the system becomes unstable. It shows that PVR-based AD method is necessary for the SRF-EPI controller to maintain stability and ensure harmonic-free grid currents.

The simulation and experimental results of the steady-state waveforms for different controllers in stationary frame with the proposed PVR-based AD method are shown in Fig. 17 and Fig. 21, respectively. As shown in Fig. 17, the fundamental RMS value of i_{ga} (A phase) in Fig. 17(a), (b) and (c) are 1.63 A, 1.422 A and 1.42A with a reference value of 1.414 A (RMS). The measured steady-state errors in Fig. 17(a), (b) and (c) are 15.3%, 0.57% and 0.42% respectively and the total harmonic distortion (THD) are 1.22%, 1.16% and 1.12%, respectively. As shown in Fig. 21, the measured steady-state errors in Fig. 21(a), (b) and (c) are consistent with simulation results. However, the current THD are 1.28%, 4.8% and 4.75%, respectively. It is noted that the THDs of the experimental results with the PR and SRF-EPI controllers are worse than that of the PI controller because the current of the PI controller has a higher amplitude due to the effect of steady state error. Therefore, the sufficient accuracy can be achieved by using SRF-EPI controller, which is slightly better than the PR controller.

The simulation and experimental results of the transient responses when the reference steps up from 1.0 kW to 2.0 kW for different controllers in stationary frame with the PVR-based AD method are shown in Fig. 18 and Fig. 22, respectively. As shown in Fig. 18, good dynamic performances are achieved when the PR and SRF-EPI controllers in the $\alpha\beta$ frame are adopted. Fig. 22 shows that the transient response of the SRF-EPI controller is slightly better than PR controller. The experimental results are consistent and in good agreement with the theoretical analysis and simulation results.

In order to evaluate the robustness of the SRF-EPI control scheme with the PVR-based AD method, the simulation and experimental results under different virtual parallel damping resistance in case of control delay and the effect of grid voltage harmonics are presented.

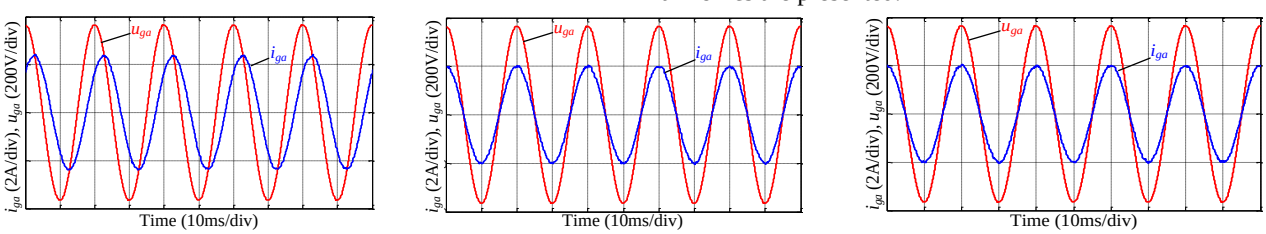

Fig. 17. Steady-state simulation results under 50% load condition with the proposed PVR-based AD strategy. (a) The PI controller. (b) The PR controller. (c) The SRF-EPI controller.

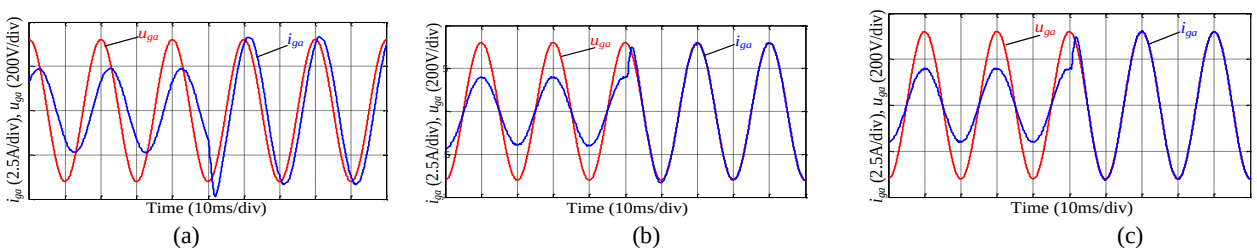

Fig. 18. Transient responses when the reference of i_{ga} steps up from half-load to full-load with the proposed PVR-based AD strategy. (a) The PI controller. (b) The PR controller. (c) The SRF-EPI controller.

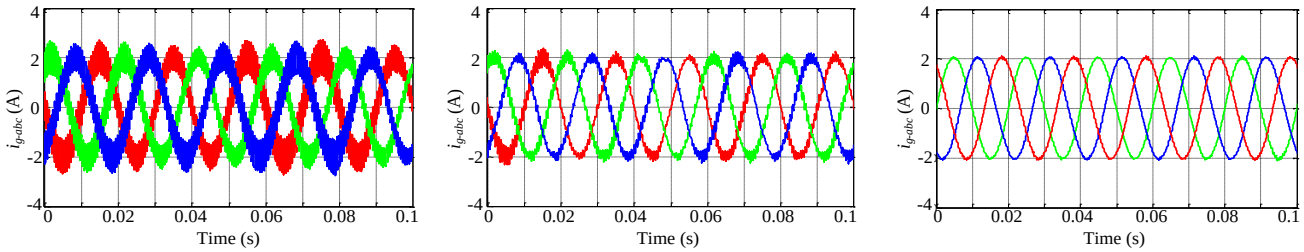

(a) (b) (c)

Fig. 19. Simulation results of different $R_{d,eq}$ with the delay time T_d=1.5T_s when the SRF-EPI controller is used in the proposed PVR-based AD strategy. (a) $R_{d,eq}$ =26.8. (b) $R_{d,eq}$ =18.8. (c) $R_{d,eq}$ =6.8.

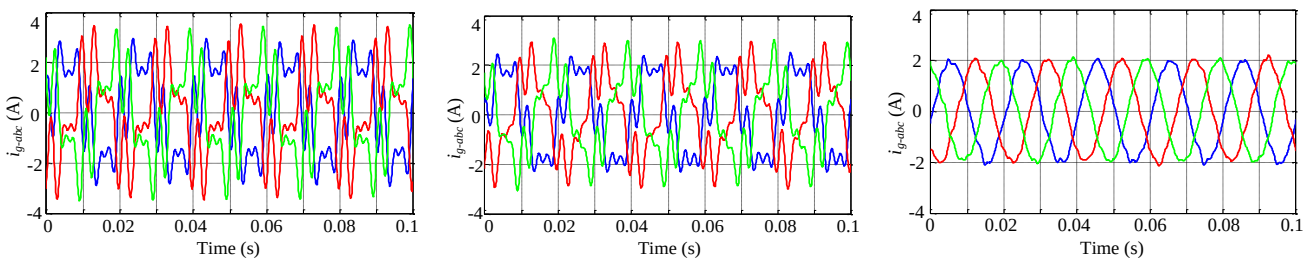

(a) (b) (c)

Fig. 20. Simulation results of the SRF-EPI controller with PVR-based AD strategy when grid voltages are highly distorted. (a) Without grid voltage feed-forward control. (b) With grid voltage feed-forward control. (c) Combine with resonant controllers and grid voltage feed-forward control.

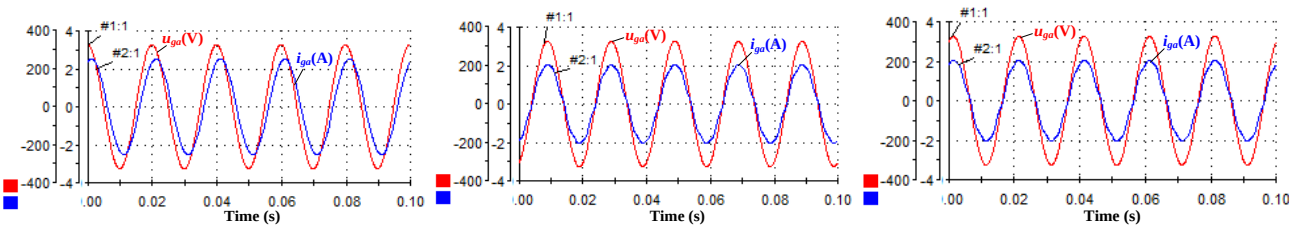

(a) (b) (c)

Fig. 21. Steady-state experimental results under half-load condition with the proposed PVR-based AD strategy. (a) The PI controller. (b) The PR controller. (c) The SRF-EPI controller.

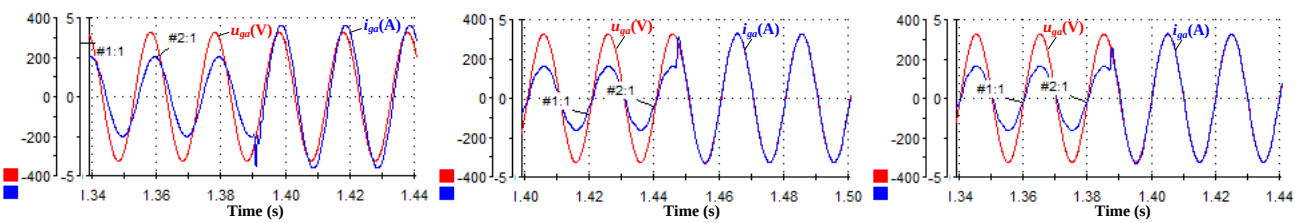

(a) (b) (c)

Fig. 22. Experimental transient waveforms when the reference of i_{ga} steps from half load to full load with the proposed PVR-based AD strategy. (a) The PI controller. (b) The PR controller. (c) The SRF-EPI controller.

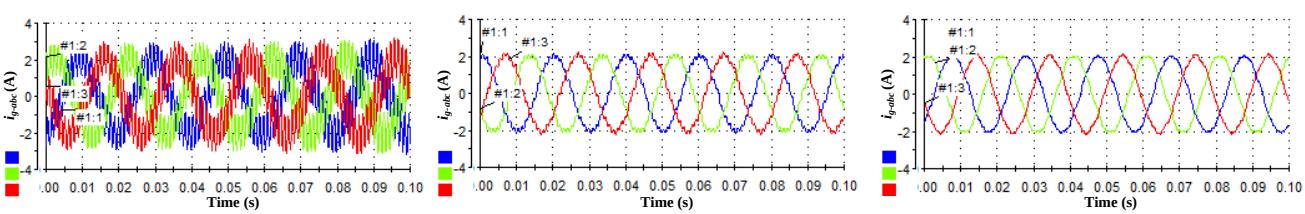

(a) (b) (c)

Fig. 23. Experimental results of different $R_{d,eq}$ with the delay time T_d=1.5T_s when the SRF-EPI controller is used in the proposed PVR-based AD strategy. (a) $R_{d,eq}$ =26.8. (b) $R_{d,eq}$ =18.8. (c) $R_{d,eq}$ =6.8.

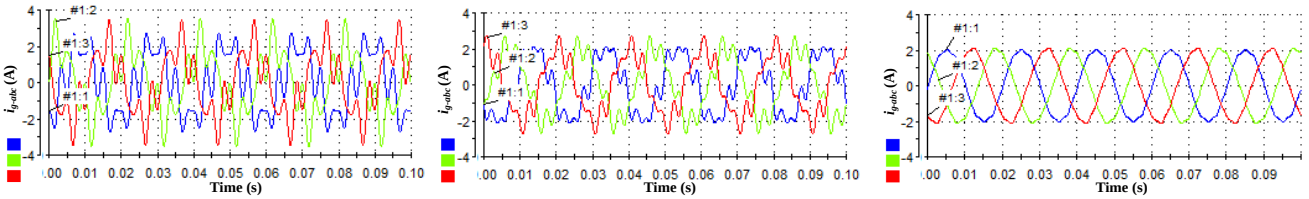

(a) (b) (c)

Fig. 24. Experimental results of the SRF-EPI controller in stationary frame with the PVR-based AD strategy when the grid voltages are highly distorted. (a) The SRF-EPI controller without grid voltage feed-forward control. (b) The SRF-EPI controller with grid voltage feed-forward control. (c) The SRF-EPI controller combines with the resonant controllers and grid voltage feed-forward control.

Fig. 19 and Fig. 23 show the effect of the feedback gain $R_{d,eq}$ of the PVR-based AD method on the output current quality with the control delay time of T_d=1.5T_s, and $R_{d,eq}$ of the SRF-EPI controller is chosen to be 26.8, 18.8 and 6.8, respectively. The simulation and experimental results under different $R_{d,eq}$ with T_d=1.5T_s are shown in Fig. 19 and Fig. 23, respectively. Although the system is stable, the harmonic content increases dramatically when the value of $R_{d,eq}$ increases and the current THDs (phase A) in Fig. 19 (a), (b) and (c) are 35.82%, 6.04%, 2.95%, respectively. The current THDs (phase A) of the experimental results in Fig. 23(a), (b) and (c) are 45%, 6.5% and 3.6%, respectively. Therefore, it is necessary to optimize the value of $R_{d,eq}$ to ensure a sufficient stability margin and a good dynamic response when the control delay is introduced.

To validate the performance of the control algorithm in case of distorted grid conditions, the grid-emulator was distorted with 5th and 7th harmonics, with voltage THDs of 3% and 2%, respectively. The simulation and experimental results of the grid currents with the SRF-EPI controller in stationary frame under different control scenarios are shown in Fig. 20 and Fig. 24, respectively. The multiple resonant controllers tuned at 5th and 7th harmonic with K_{ih}=5 for h=5 and 7 are added to the SRF-EPI controller in stationary frame with the proposed active damping method. The THDs of simulated grid current i_{ga} under different control scenarios are shown in Fig. 20, which are 64.27%, 38.33%, 3.22%, respectively. As shown in Fig. 24, the current THDs of the experimental results are about 54.38%, 29.12% and 3.92%, respectively. It shows that when only the SRF-EPI controller is used, the grid currents are highly distorted due to harmonic distortion of grid voltages. When the grid voltage feed-forward scheme is used in combination with proposed control strategies, the current distortion can be effectively suppressed. However, the THD of the grid current is still high and the distortion in grid currents cannot be rejected by the voltage feed-forward loop alone. However, when the SRF-EPI controller is adopted in combination with the grid voltage feed-forward loop and the multiple resonant controllers in the current loop, the sinusoidal waveforms are guaranteed in the grid currents.

V. Conclusions

In this paper, the stationary frame SRF-EPI control algorithm using PVR-based AD method is proposed for three-phase *LCL* type grid-connected DG system, which achieves a compromise between the resonance damping and the dynamic performance and makes it easier to stabilize the whole system. The accurate stationary frame of SRF-EPI controller is introduced to achieve a high closed-loop bandwidth and good robustness. It is found that the SRF-EPI controller is equivalent to the PR controller in stationary frame at fundamental frequency, but shows different phase characteristics at other frequency ranges compared to the PR or PI controller in the stationary frame.

In order to guarantee the quality of the grid currents under non-ideal grid conditions, the grid voltage feed-forward control with the multiple resonant controllers in harmonic frequencies is adopted, and the performance under no damping, PD and AD methods are compared. Furthermore, the design guidelines of whole system of the SRF-EPI, PI and PR controllers are presented. Finally, simulation and experimental results of a three-phase *LCL*-based grid-connected inverter are presented to validate the proposed control approach.

Acknowledgment

This work was supported by the National Natural Science Foundation of China (51307015), and the State Key Laboratory of Power Transmission Equipment & System Security and New Technology, Chongqing University (2007DA10512713405), and the Open Research Subject of Sichuan Province Key Laboratory of Power Electronics Energy-Saving Technologies & Equipment (szjj2015-067), and by the Open Research Subject of Artificial Intelligence Key Laboratory of Sichuan Province (2015RZJ02).

References

[1] F. Blaabjerg, R. Teodorescu, M. Liserre, and A. Timbus, "Overview of control and grid synchronization for distributed power generation systems," *IEEE Trans. Ind. Electron.*, vol. 53, no. 5, pp. 1398–1409, Oct. 2006.

[2] P. Sivakumar, and M. S. Arutchelvi, "Enhanced controller topology for photovoltaic sourced grid connected inverters under unbalanced nonlinear loading," *Journal of Power Electron.*, vol. 14, no. 2, pp. 369–382, Mar. 2014.

[3] L. Zhang, K. Sun, Y. Xing, and M. Xing, "H6 transformerless full-bridge PV grid-tied inverters," *IEEE Trans. Power Electron.*, Vol. 29, No. 3, pp. 1229-1238, Mar. 2014.

[4] L. Zhang, K. Sun, H. Hu, and Y. Xing, "A system-level control strategy of photovoltaic grid-tied generation systems for european efficiency enhancement," *IEEE Trans. Power Electron.*, Vol. 29, No. 7, pp. 3445-3453, Jul. 2014.

[5] J. He, and Y. W. Li, "Generalized closed-loop control schemes with embedded virtual impedances for voltage source converters with LC or LCL filters," *IEEE Trans. Power Electron.*, vol. 27, no. 4, pp. 1850–1861, Apr. 2012.

[6] S. Guoqiao, Z. Xuancai, Z. Jun, and X. Dehong, "A new feedback method for PR current control of LCL-filter-based grid-connected inverter," *IEEE Trans. Ind. Electron.*, vol. 57, no. 6, pp. 2033–2041, Jun. 2010.

[7] J. Dannehl, M. Liserre, and F. W. Fuchs, "Filter-based active damping of voltage source converters with filter," *IEEE Trans. Ind. Electron.*, vol. 58, no. 8, pp. 3623–3633, Aug. 2011.

[8] R. Pena-Alzola, M. Liserre, F. Blaabjerg, R. Sebastian, J. Dannehl, and F. W. Fuchs, "Analysis of the passive damping losses in LCL-filter-based grid converters," *IEEE Trans. Power Electron.*, vol. 28, no. 6, pp. 2642–2646, Jun. 2013.

[9] R. Beres, X. Wang, F. Blaabjerg, C. L. Bak, and M. Liserre, "Comparative evaluation of passive damping topologies for parallel grid-connected converters with LCL filters," in *Proc. IEEE Power Electron. May. Conf.*, 2014, pp. 3320–3327.

[10] J. Xu, S. Xie, and T. Tang, "Active damping-based control for grid-connected LCL-filtered inverter with injected grid current feedback only," *IEEE Trans. Ind. Electron.*, vol. 61, no. 9, pp. 4746–4758, Sep. 2014.

[11] C. P. Dick, S. Richter, M. Rosekeit, J. Rolink, and R. W. De Doncker, "Active damping of LCL resonance with minimum sensor effort by means of a digital infinite impulse response filter," in *Proc. IEEE Power Electron. Sept. Conf.*, 2007, pp. 1–8.

[12] G. Shen, D. Xu, L. Cao, and X. Zhu, "An improved control strategy for grid-connected voltage source inverters with a LCL filter," *IEEE Trans. Power Electron.*, vol. 43, no. 5, pp. 1899–1906, Jul. 2008.

[13] J. Dannehl, F. W. Fuchs, S. Hansen, and P. B. Thøgersen, "Investigation of active damping approaches for PI-based current control of grid-connected pulse width modulation converters with LCL filters," *IEEE Trans. Ind. Appl.*, vol. 46, no. 4, pp. 1509–1517, Jul./Aug. 2010.

[14] C. Bao, X. Ruan, X. Wang, W. Li, D. Pan, and K. Weng, "Step-by-step controller design for LCL-type grid-connected inverter with capacitor–current-feedback active-damping," *IEEE Trans. Power Electron.*, vol. 29, no. 3, pp. 1239–1253, Mar. 2014.

[15] S. G. Parker, B. P. McGrath, and D. G. Holmes, "Regions of active damping control for LCL filters," *IEEE Trans. Ind. Appl.*, vol. 50, no. 1, pp. 424–432, Jan./Feb. 2014.

[16] M. Hanif, V. Khadkikar, W. Xiao, and J. L. Kirtley, "Two degrees of freedom active damping technique for filter-based grid connected PV systems," *IEEE Trans. Ind. Electron.*, vol. 61, no. 6, pp. 2795–2803, Jun. 2014.

[17] Y. Lei, W. Xu, C. Mu, and Z. Zhao, "New hybrid damping strategy for grid-connected photovoltaic inverter with LCL filter," *IEEE Trans. Appl. Supercond.*, vol. 24,no. 5, pp. 361–368, Aug. 2014.

[18] J. C. Vasquez, J. M. Guerrero, M. Savaghebi, J. Eloy-Garcia, and R. Teodorescu, "Modeling, analysis, and design of stationary-reference-frame droop-controlled parallel three-phase voltage source inverters," *IEEE Trans. Ind. Electron.*, vol. 60, no. 4, pp. 1271–1280, Apr. 2013.

[19] N. He, D. Xu, Y. Zhu, J. Zhang, G. Shen, Y. Zhang, J. Ma, and C. Liu, "Weighted average current control in a three-phase grid inverter with an LCL filter," *IEEE Trans. Power Electron.*, vol. 28, no. 6, pp. 2785–2797, Jun. 2013.

[20] X. Yuan, W. Merk, H. Stemmler, and J. Allmeling, "Stationary-frame generalized integrators for current control of active power filters with zero steady-state error for current harmonics of concern under unbalanced and distorted operating conditions," *IEEE Trans. Ind. Appl.*, vol. 38, no. 2, pp. 523–532, Mar./Apr. 2002.

[21] H. Yi, F. Zhuo, Y. Li, Y. Zhang, and W. Zhan, "Comparison analysis of resonant controllers for current regulation of selective active power filter with mixed current reference," *Journal of Power Electron.*, vol. 13, no. 5, pp. 861–876, Sept. 2013.

[22] Y. Jia, J. Zhao, and X. Fu, "Direct grid current control of LCL filtered grid-connected inverter mitigating grid voltage disturbance," *IEEE Trans. Power Electron.*, vol. 29, no. 3, pp. 1532–1541, Mar. 2014.

[23] M. A. Abusara, S. M. Sharkh, and P. Zanchetta, "Control of grid-connected inverters using adaptive repetitive and proportional resonant schemes," *Journal of Power Electron.*, vol. 15, no. 2, pp. 518–529, Mar. 2015.

[24] X. Bao, F. Zhuo, Y. Tian, and P. Tan, "Simplified feedback linearization control of three-phase photovoltaic inverter with an LCL filter," *IEEE Trans. Power Electron.*, vol. 28, no. 6, pp. 2739–2752, Jun. 2013.

[25] T. Yi, L. Poh Chiang, W. Peng, C. Fook Hoong, and G. Feng, "Exploring inherent damping characteristic of LCL-filters for three-phase grid-connected voltage source inverters," *IEEE Trans. Power Electron.*, vol. 27,no. 3, pp. 1433–1443, Mar. 2012.

[26] C. Zou, Liu, S. Duan, and R. Li, "Stationary frame equivalent model of proportional-integral controller in *dq* synchronous frame," *IEEE Trans. Power Electron.*, vol. 29,no. 9, pp. 4461–4465, Sept. 2014.

[27] G. Shen, X. Zhu, J. Zhang, and D. Xu, "A new feedback method for PR current control of LCL-filter-based grid-connected inverter," *IEEE Trans. Ind. Electron.*, vol. 57, no. 6, pp. 2033–2041, Jun. 2010.

[28] N. Zmood, and D. G. Holmes, "Stationary frame current regulation of PWM inverters with zero steady-state error," *IEEE Trans. Power Electron.*, vol. 18, no. 3, pp. 814–822, May. 2003.

[29] C. Zou, B. Liu, and R. Li, "Influence of delay on system stability and delay optimization of grid-connected inverters with LCL filter," *IEEE Trans. Ind. Inform.*, vol. 10, no. 3, pp. 1775–1784, Aug. 2014.

[30] J. Xu, S. Xie, and T. Tang, "Evaluations of current control in weak grid case for grid-connected LCL-filtered inverter," *IET Power Electron.*, vol. 6, no. 2, pp. 227–234, Feb. 2013.

[31] D. A. Timbus, M. Liserre, R. Teodorescu, P. Rodriguez, and F. Blaabjerg, "Evaluation of current controller for distributed power generation systems," *IEEE Trans. Power Electron.*, vol. 24, no. 3, pp. 654–664, Mar. 2009.

[32] T. Abeyasekera, C. M. Johnson, D. J. Atkinson, and M. Armstrong, "Suppression of line voltage related distortion in current controlled grid connected inverters," *IEEE Trans. Power Electron.*, vol. 20, no. 6, pp. 1393–1401, Nov. 2005.

[33] X. Wang, X. Ruan, S. Liu, and C. K. Tse, "Full feedforward of grid voltage for grid-connected inverter with LCL filter to suppress current distortion due to grid voltage

harmonics," *IEEE Trans. Power Electron.*, vol. 25, no. 12, pp. 3119–3127, Dec. 2010.

[34] K. Jalili and S. Bernet, "Design of LCL filters of active-front-end twolevel voltage-source converters," *IEEE Trans. Ind. Electron.*, vol. 56, no. 5, pp. 1674–1689, May. 2009.

Yang Han was born in Chengdu, China. He received his Ph.D. in Electrical Engineering from Shanghai Jiaotong University (SJTU), Shanghai, China, in 2010. He joined the Department of Power Electronics, School of Mechatronics Engineering, University of Electronic Science and Technology of China (UESTC) in 2010, and where he has been an Associate Professor since 2013. From March 2014 to March 2015, he was a Visiting Scholar at the Department of Energy Technology, Aalborg University, Aalborg, Denmark. His research interests include ac/dc microgrids, power quality, grid-connected converters for renewable and DGs, active power filters and static synchronous compensators (STATCOMs). He has authored more than 20 ISI-indexed journal papers in the area of power electronics, power quality conditioners, and smart grid. He received Best Paper Awards from 2013 Annual Conference of HVDC and Power Electronics Committee of Chinese Society of Electrical Engineers (CSEE) in Chongqing, China, and the 4th International Conference on Power Quality in 2008, in Yangzhou, China.

Pan Shen was born in Hefei, China. He received his B.S. in Electrical Engineering and Automation from Anhui Agricultural University, Hefei, China, in 2013. He is currently working toward the M.S. degree in Power Electronics and Electric Drives at the University of Electronic Science and Technology of China (UESTC), Chengdu, China. His current research interests include power quality, power converters, ac/dc microgrid, power system automation, and active power filters.

Josep M. Guerrero received the B.S. degree in telecommunications engineering, the M.S. degree in electronics engineering, and the Ph.D. degree in power electronics from the Technical University of Catalonia, Barcelona, in 1997, 2000 and 2003, respectively. Since 2011, he has been a Full Professor with the Department of Energy Technology, Aalborg University, Denmark, where he is responsible for the Microgrid Research Program. From 2012 he is a guest Professor at the Chinese Academy of Science and the Nanjing University of Aeronautics and Astronautics; from 2014 he is chair Professor in Shandong University; and from 2015 he is a distinguished guest Professor in Hunan University. His research interests is oriented to different microgrid aspects, including power electronics, distributed energy-storage systems, hierarchical and cooperative control, energy management systems, and optimization of microgrids and islanded minigrids. He is an Associate Editor for the IEEE TRANSACTIONS ON POWER ELECTRONICS, the IEEE TRANSACTIONS ON INDUSTRIAL ELECTRONICS, and the IEEE Industrial Electronics Magazine, and an Editor for the IEEE TRANSACTIONS on SMART GRID and IEEE TRANSACTIONS on ENERGY CONVERSION. He has been Guest Editor of the IEEE TRANSACTIONS ON POWER ELECTRONICS Special Issues: Power Electronics for Wind Energy Conversion and Power Electronics for Microgrids; the IEEE TRANSACTIONS ON INDUSTRIAL ELECTRONICS Special Sections: Uninterruptible Power Supplies systems, Renewable Energy Systems, Distributed Generation and Microgrids, and Industrial Applications and Implementation Issues of the Kalman Filter; and the IEEE TRANSACTIONS on SMART GRID Special Issue on Smart DC Distribution Systems. He was the chair of the Renewable Energy Systems Technical Committee of the IEEE Industrial Electronics Society. In 2014 he was awarded by Thomson Reuters as Highly Cited Researcher, and in 2015 he was elevated as IEEE Fellow for his contributions on "distributed power systems and microgrids."